

Industrial Chemistry & Materials

Accepted Manuscript

This article can be cited before page numbers have been issued, to do this please use: X. Zhang, C. Su, R. Shi, M. Li, L. Fu, R. Liu, Y. Chen, B. Li and G. Zhang, *Ind. Chem. Mater.*, 2025, DOI: 10.1039/D5IM00296F.



This is an Accepted Manuscript, which has been through the Royal Society of Chemistry peer review process and has been accepted for publication.

Accepted Manuscripts are published online shortly after acceptance, before technical editing, formatting and proof reading. Using this free service, authors can make their results available to the community, in citable form, before we publish the edited article. We will replace this Accepted Manuscript with the edited and formatted Advance Article as soon as it is available.

You can find more information about Accepted Manuscripts in the [Information for Authors](#).

Please note that technical editing may introduce minor changes to the text and/or graphics, which may alter content. The journal's standard [Terms & Conditions](#) and the [Ethical guidelines](#) still apply. In no event shall the Royal Society of Chemistry be held responsible for any errors or omissions in this Accepted Manuscript or any consequences arising from the use of any information it contains.

ARTICLE

Electron-Withdrawing Pyridine-Functionalized g-C₃N₄-Coordinated Cobalt Phthalocyanine for Enhanced Photocatalytic CO₂ Reduction

Xuehua Zhang,^{af} Chunlei Su,^{af} Rui Shi,^b Mingming Li,^c Lili Fu,^d Rongji Liu,^e Yong Chen,^{*b} Bin Li^{*d} and Guangjin Zhang,^{*af}

Received 00th January 20xx,
Accepted 00th January 20xx

DOI: 10.1039/x0xx00000x

To enhance the charge separation efficiency of g-C₃N₄ and facilitate electron transfer between photosensitizer and molecular catalyst, polarization and coordination strategies are taken by grafting pyridine rings onto the edge of g-C₃N₄ framework. Herein, electron-withdrawing pyridine edge-functionalized g-C₃N₄ (g-C₃N₄-P_x) was synthesized via a facile one-step thermal polymerization of urea and 4-aminopyridine, and employed as visible-light photosensitizer hybridized with cobalt phthalocyanine (CoPc) for efficient photoreduction of CO₂. Both experimental and theoretical results confirm that electron-withdrawing pyridine grafting facilitates in-plane charge separation and directs electron migration toward the edge of g-C₃N₄, narrows its band gap for enhanced visible-light absorption, and provides dynamic coordination sites that significantly boost interfacial electron transfer from g-C₃N₄-P_x to CoPc. A significant enhancement in CO yield was achieved with the optimized CoPc/g-C₃N₄-P_{1.5} hybrid, reaching 14.95 mmol g⁻¹ after 6 hours of visible-light irradiation—a 6.1-fold improvement over the unmodified CoPc/g-C₃N₄ (2.47 mmol g⁻¹). This work paves a facile approach for developing highly efficient hybrid photocatalysts for CO₂ reduction and improving the charge separation and visible light absorption in organic semiconductors.

Keywords: CO₂ photoreduction; Cobalt phthalocyanine/g-C₃N₄ hybrid photocatalysts; Polarization engineering; Directional electron transfer; Coordination interaction; Electron-withdrawing effect.

1. Introduction

Photocatalytic carbon dioxide (CO₂) reduction using solar energy represents an ideal approach to address energy and environmental challenges, as it operates under ambient conditions and produces value-added chemicals.¹⁻³ Despite widespread interest, achieving high selectivity and efficiency in CO₂ photoreduction remains challenging due to thermodynamic and kinetic limitations.⁴⁻⁶ The inherent stability of CO₂ molecule, competitive hydrogen evolution reactions in aqueous environments, limited solar spectrum absorption, and severe charge carrier recombination—especially in single-component systems—further hinder the progress. Thus, developing highly active and selective hybrid photocatalysts is essential.

A promising strategy involves hybrid systems comprising a visible-light-absorbing semiconductor sensitizer and a metal molecular catalyst with high CO₂ reduction activity.⁷⁻²³ Recent studies have explored various hybrids, such as ruthenium(II)-complex-modified graphitic carbon nitride (g-C₃N₄) for formate production, and Iron (Fe) or cobalt (Co) molecular catalysts coupled with g-C₃N₄, cadmium sulphide (CdS), or related semiconductors for photoreduction of CO₂ to carbon monoxide (CO).⁹⁻¹⁷ In these systems, spatial separation between the light absorber and catalytic centre promotes charge separation and enhances CO₂ reduction performance. Consequently, enhancing both the semiconductor's light-harvesting capacity and its interaction with the molecular catalyst is critical for increasing photon utilization and facilitating electron transfer.^{24,25}

^a CAS Key Laboratory of Green Process and Engineering, Institute of Process Engineering, Chinese Academy of Sciences, Beijing, 100190, China. E-mail: zhanggj@ipe.ac.cn

^b Key Laboratory of Photochemical Conversion and Optoelectronic Materials, Technical Institute of Physics and Chemistry, Chinese Academy of Sciences, Beijing 100190, China. E-mail: chenrong@mail.ipc.ac.cn

^c National Center for Nanoscience and Technology, Beijing 100190, China.

^d Zhengzhou Tobacco Research Institute of CNTC, Zhengzhou, 450001, China. E-mail: lib@ztri.com.cn

^e Department of Chemistry, Johannes Gutenberg University Mainz, Duesbergweg 10-14, 55128 Mainz, Germany.

^f Center of Materials Science and Optoelectronics Engineering, Chinese Academy of Sciences, Beijing, 100049, China

[†] Electronic Supplementary Information (ESI) available. See DOI: 10.1039/x0xx00000x



Efforts to accelerate electron transfer from photosensitizers to catalysts have led to covalent linker strategies, like direct connection, ethylene or amide bonds,^{13,14,26,27} however, these often involve complex synthesis and may suffer from back electron transfer, compromising activity and stability. As a covalent bond, coordination bond can be an ideal intermolecular force to realize the connection between photosensitizer and catalyst. The unstable characteristics of coordination bonds will give dynamic stability. At the same time, the coordination interaction is expected to realize the inner shell electron transfer, thus overcoming the limitation of diffusion rate and promoting the electron transfer between molecules. Moreover, dynamic coordination interactions offer reversible and self-correcting binding, which can improve durability of the hybrids.²⁰

As an organic semiconductor, g-C₃N₄ has attracted significant attention for various application due to its facile synthesis, suitable band alignment, good stability, visible light response and layered structure.²⁸⁻³² Nonetheless, pristine g-C₃N₄ suffers from rapid charge recombination and restricted visible-light absorption, limiting its photocatalytic activity. Strategies such as defect engineering, elemental doping, heterojunction construction, and metal deposition have been employed to address these issues.³³⁻³⁵ Regulating molecular polarity has also emerged as an effective route to promote intramolecular charge transfer and narrow the bandgap of g-C₃N₄.³⁶⁻³⁸ Additionally, coupling g-C₃N₄ with molecular catalysts like cobalt phthalocyanine (CoPc)—known for its high selectivity in CO₂-to-CO conversion^{39,40}—offers a pathway toward efficient CO₂ reduction, with CO serving as a key industrial feedstock for synthetic fuels and chemicals.

In this work, we introduce polarization engineering and dynamic coordination strategies to enhance the in-plane charge separation in g-C₃N₄ and provide reversible coordination binding sites for CoPc molecular catalysts. Pyridine edge-functionalized g-C₃N₄ (g-C₃N₄-P_x) was designed and synthesized as a light absorber (Scheme S1). The electron-withdrawing pyridine groups can promote the formation of a donor–acceptor structure, narrow the bandgap and improve the visible-light absorption and charge separation. More importantly, the pyridine edges can offer dynamic axial coordination sites for CoPc,⁴¹⁻⁴³ facilitating interfacial electron transfer from the light harvesting part g-C₃N₄ to the catalytic site CoPc. Through the synergistic effect of polarization engineering and dynamic coordination, efficient charge separation and transfer are realized, and ultimately the photocatalytic performance of the CoPc/g-C₃N₄-P_x hybrid catalyst for CO₂ reduction is enhanced.

2. Results and discussion

2.1 Structure and morphology

The pyridine edge-functionalized g-C₃N₄-P_x samples were prepared through a facile one-step homogeneous thermal polymerization of urea with different amount of 4-aminopyridine.³⁶ The possible polymerization reaction is proposed in Scheme S2. Fig. 1a presents the X-ray diffraction (XRD) patterns of pristine g-C₃N₄ and g-C₃N₄-P_x samples, x is the weight percentage of 4-aminopyridine relative to urea used during synthesis. All XRD patterns exhibit the characteristic diffraction peaks of g-C₃N₄ at 2θ = 12.8° and 27.6°, corresponding to the (100) in-plane structure and the (002) interlayer stacking, respectively. Notably, no significant shift is observed in the positions of these diffraction peaks in the g-C₃N₄-P_x samples compared to pristine g-C₃N₄, indicating that pyridine functionalization at the edges does not alter the crystalline and layered structure of g-C₃N₄. Fig. 1b displays the N₂ adsorption-desorption isotherms of g-C₃N₄ and g-C₃N₄-P_x samples. All materials show type IV isotherm with H3 hysteresis, indicative of mesoporous structures. The Brunauer-Emmett-Teller (BET) specific surface areas are measured to be 80.2, 78.0, 75.4, 75.6, 72.7 and 57.6 m² g⁻¹ for g-C₃N₄, g-C₃N₄-P_{0.5}, g-C₃N₄-P_{1.0}, g-C₃N₄-P_{1.5}, g-C₃N₄-P_{2.0} and g-C₃N₄-P_{3.0}, respectively.

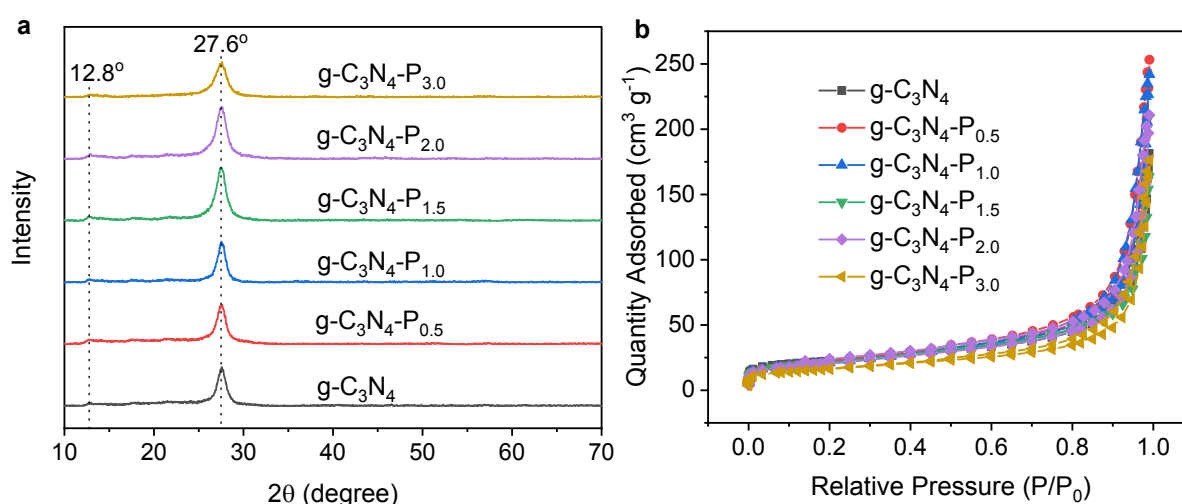


Fig. 1 (a) XRD patterns and (b) N₂ adsorption-desorption isotherms of the pristine g-C₃N₄ and g-C₃N₄-P_x (x = 0.5 ~ 3.0) samples.



The morphology of pristine $g\text{-C}_3\text{N}_4$ and the as-synthesized $g\text{-C}_3\text{N}_4\text{-P}_x$ samples were characterized using scanning electron microscope (SEM) (Fig. 2a-2f) and transmission electron microscope (TEM) (Fig. 2g-2j). All the samples exhibit mesoporous sheet morphology. Specifically, $g\text{-C}_3\text{N}_4$, $g\text{-C}_3\text{N}_4\text{-P}_{0.5}$, $g\text{-C}_3\text{N}_4\text{-P}_{1.0}$, and $g\text{-C}_3\text{N}_4\text{-P}_{1.5}$ display relatively predominantly ultrathin, flaky, and porous structures. In contrast, $g\text{-C}_3\text{N}_4\text{-P}_{2.5}$ and $g\text{-C}_3\text{N}_4\text{-P}_{3.0}$ —which feature a higher content of edge-grafted pyridine—show increasingly aggregated and thicker sheet-like structures that appear less prone to exfoliation. Representative TEM images of $g\text{-C}_3\text{N}_4$, $g\text{-C}_3\text{N}_4\text{-P}_{0.5}$, $g\text{-C}_3\text{N}_4\text{-P}_{1.5}$ and $g\text{-C}_3\text{N}_4\text{-P}_{3.0}$ are presented in Fig. 2g–2j. These images reveal that $g\text{-C}_3\text{N}_4$, $g\text{-C}_3\text{N}_4\text{-P}_{0.5}$ and $g\text{-C}_3\text{N}_4\text{-P}_{1.5}$ maintain a flaky and ultrathin nanosheet structure, whereas $g\text{-C}_3\text{N}_4\text{-P}_{3.0}$ exhibits slightly thicker sheets. Both SEM and TEM results confirm that the edge functionalization with pyridine does not disrupt the fundamental lamellar porous structure of $g\text{-C}_3\text{N}_4$, consistent with the XRD patterns shown in Fig. 1. Samples with low levels of edge-pyridine functionalization ($g\text{-C}_3\text{N}_4\text{-P}_x$, $x = 0 \sim 2.0$) exhibit relatively high surface areas, attributed to their flaky and porous morphology, which slightly decreases as the amount of the pyridine grafting increases. In contrast, $g\text{-C}_3\text{N}_4\text{-P}_{3.0}$, with a high degree of functionalization, shows a marked decrease in surface area ($57.6 \text{ m}^2 \text{ g}^{-1}$), likely due to the aggregate thick feature as observed in SEM and TEM images.

The chemical composition and electronic states of the samples were further analysed by X-ray photoelectron spectroscopy (XPS). The XPS survey spectra in Fig. S1a confirm the presence of C and N in all $g\text{-C}_3\text{N}_4\text{-P}_x$ materials, while XPS survey spectra in Fig. S1b confirm the successful hybrid of CoPc and $g\text{-C}_3\text{N}_4\text{-P}_{1.5}$. The small O peak appearing at 532.1 eV is attributed to the adsorbed H_2O . High-resolution of C 1s, N 1s and Co 2p spectra are presented in Fig. S2, Fig. 3 a and Fig. 3b respectively. The C 1s spectrum displays two peaks at 284.8 eV (graphitic carbon, C-C/C=C) and 288.1 eV (sp^2 -hybridized carbon in N-C=N/C-N=C groups).⁴⁴ The N 1s spectrum can be deconvoluted into three components: pyridinic N (C-N=C) at 398.5–399.6 eV, pyrrolic N (tertiary N-C_3) at 399.8–399.9 eV, and terminal amino groups ($-\text{NH}_2/\text{NH}$) at 401.2 eV.⁴⁵ While the C 1s spectrum remains unchanged after pyridine modification (Fig. S2), the N 1s peaks corresponding to pyridinic and pyrrolic nitrogen shift slightly to higher binding energy (from 398.5 to 398.7 eV and from 399.8 to 400.1 eV, respectively) after grafting pyridine, suggesting reduced electron density around nitrogen atoms due to the electron-withdrawing effect of grafted pyridine. The Co 2p spectrum displays two peaks at 793.2 eV (Co $2p_{1/2}$) and 777.6 eV (Co $2p_{3/2}$) in CoPc. However, the formation of the CoPc/ $g\text{-C}_3\text{N}_4\text{-P}_{1.5}$ hybrid causes the Co $2p_{1/2}$ and Co $2p_{3/2}$ peaks shift to lower binding energy 792.4 eV and 776.8 eV, respectively. This indicates an increase in electron density of the Co site because of the electrons flow from $g\text{-C}_3\text{N}_4\text{-P}_{1.5}$ to CoPc.

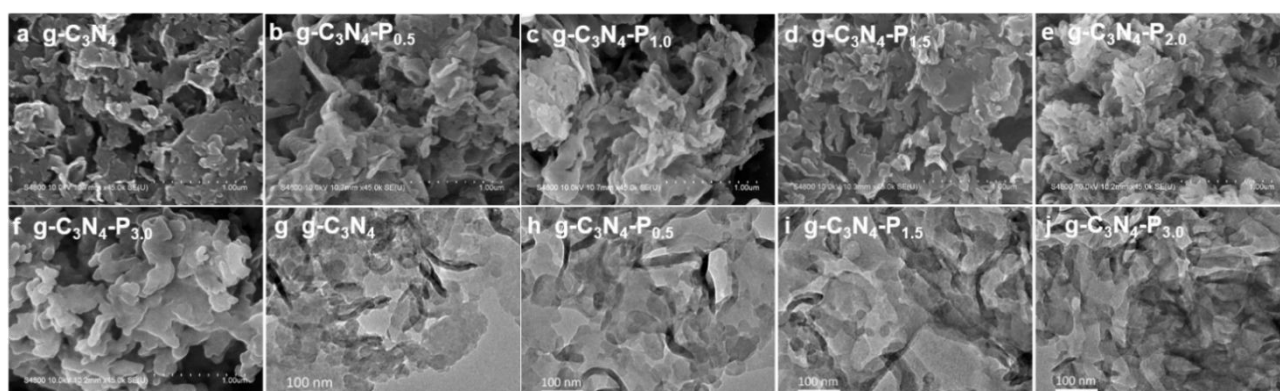


Fig. 2 (a-f) SEM and (g-j) TEM images of the pristine $g\text{-C}_3\text{N}_4$ and $g\text{-C}_3\text{N}_4\text{-P}_x$ ($x = 0.5 \sim 3.0$) samples.

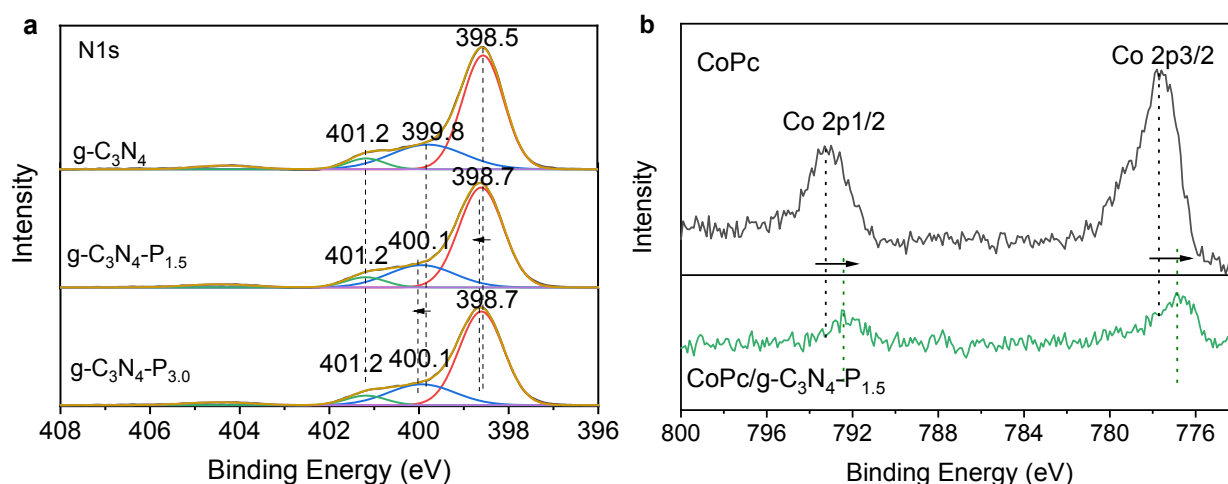


Fig. 3 High resolution XPS spectra of (a) N 1s of $g\text{-C}_3\text{N}_4$, $g\text{-C}_3\text{N}_4\text{-P}_{1.5}$, and $g\text{-C}_3\text{N}_4\text{-P}_{3.0}$ samples, (b) Co 2p of CoPc and CoPc/ $g\text{-C}_3\text{N}_4\text{-P}_{1.5}$ hybrid catalyst.



2.2 Optical properties and band structures

The optical properties of pristine g-C₃N₄ and pyridine-modified g-C₃N₄-P_x samples were investigated using UV-vis diffuse reflectance spectroscopy (UV-vis DRS) measurements. As shown in Fig. 4a, the absorption intensity in the visible region initially increases and then decreases, with g-C₃N₄-P_{1.5} exhibiting the strongest absorption between 380 and 450 nm. Concurrently, the absorption edge progressively red-shifts from g-C₃N₄ to g-C₃N₄-P_{3.0} as the pyridine content increases. Samples g-C₃N₄-P_{1.5}, g-C₃N₄-P_{2.0} and g-C₃N₄-P_{3.0} demonstrate significantly enhanced visible light absorption compared to unmodified g-C₃N₄.

The band gaps (E_g) of the samples, determined via the Kubelka–Munk method (Fig. S3), are 2.80 eV (g-C₃N₄), 2.77 eV (g-C₃N₄-P_{0.5}), 2.74 eV (g-C₃N₄-P_{1.0}), 2.68 eV (g-C₃N₄-P_{1.5}), 2.50 eV (g-C₃N₄-P_{2.0}), and 2.07 eV (g-C₃N₄-P_{3.0}), indicating a gradual narrowing in E_g with increasing pyridine modification. This narrowing band gap is attributed to the formation of an intramolecular donor–acceptor structure within g-C₃N₄-P_x, resulting from the grafting of electron-withdrawing pyridine onto the g-C₃N₄ framework. This structure promotes intramolecular charge separation, thereby causing a red shift in the absorption edge and enhancing visible light absorption. Consistent with these changes, the powder colour deepens from light yellow to dark yellow with increasing pyridine content, as shown in Fig. S4.

Mott-Schottky measurements were conducted to determine the flat-band potentials (E_{FB}) of the synthesized g-C₃N₄ and g-C₃N₄-P_x samples. As shown in Fig. 4b, the positive slopes of the Mott-Schottky plots confirm that all samples exhibit n-type semiconductor behaviour. The E_{FB} values were obtained by extrapolating the linear region of the plots to the intercept on the X-axis (where $1/C^2 = 0$).^{46,47} The calculated E_{FB} values are −0.99, −1.03, −1.06, −1.06, −1.03 and −1.01 V (vs. NHE) for g-C₃N₄, g-C₃N₄-P_{0.5}, g-C₃N₄-P_{1.0}, g-C₃N₄-P_{1.5}, g-C₃N₄-P_{2.0}, and g-C₃N₄-P_{3.0}, respectively. For n-type semiconductors, the conduction band minimum (E_{CB}) is typically 0.1–0.3 eV higher than E_{FB} , depending on the electron effective mass and carrier concentration.^{48,49} Assuming a difference of 0.2 eV, the estimated E_{CB} values are −1.19 V, −1.23 V, −1.26 V, −1.26 V, −1.23 V, and −1.21 V (vs. NHE) for g-C₃N₄, g-C₃N₄-P_{0.5}, g-C₃N₄-P_{1.0}, g-C₃N₄-P_{1.5}, g-C₃N₄-P_{2.0}, and g-C₃N₄-P_{3.0}, respectively. The Mott-Schottky results indicate that pyridine modification at the edges has a minimal effect on both (E_{FB}) and (E_{CB}) of the g-C₃N₄-P_x materials.

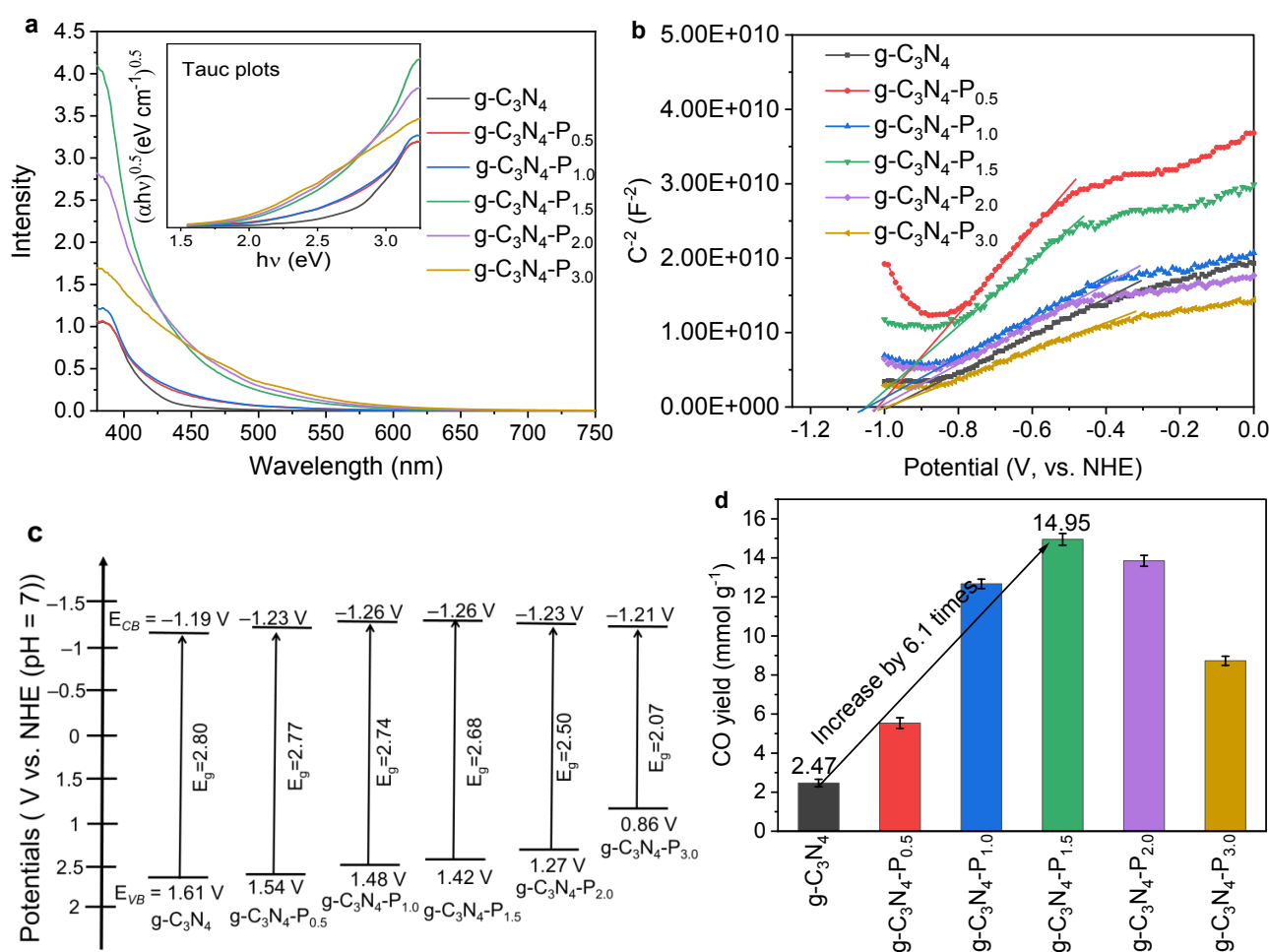


Fig. 4 (a) UV-vis DRS spectra, Tauc plots (inset), (b) Mott-Schottky plots, and (c) band structure alignments for g-C₃N₄ and g-C₃N₄-P_x ($x = 0.5 \sim 3.0$) samples; (d) CO yield from CO₂ photoreduction over g-C₃N₄ and g-C₃N₄-P_x ($x = 0.5 \sim 3.0$) coupled with CoPc in CH₃CN:H₂O:TEOA (3:1:1, 100 mL) solution after 6 h illumination, 420 nm < λ < 780 nm, 280 mW cm⁻².



Based on the E_g values derived from the Tauc plots in Fig. 4a, the valence band energy (E_{VB}) values of g-C₃N₄, g-C₃N₄-P_{0.5}, g-C₃N₄-P_{1.0}, g-C₃N₄-P_{1.5}, g-C₃N₄-P_{2.0} and g-C₃N₄-P_{3.0} were calculated to be 1.61, 1.54, 1.48, 1.42, 1.27, and 0.86 V (vs. normal hydrogen electrode, NHE), respectively. This progressive increase in E_{VB} indicates that pyridine incorporation at the edges of the g-C₃N₄ framework systematically raises the valence band level. As depicted in the band structure diagram in Fig. 4c, pyridine modification leads to a continuous reduction of the band gap from 2.80 eV to 2.07 eV, accompanied by an upward shift of the E_{VB} from 1.61 eV to 0.86 eV. In contrast, the conduction band level remains essentially unchanged, with E_{CB} values confined within a narrow range of -1.19 V to -1.26 V—a variation of only 0.02–0.07 V across all samples. This stability in the conduction band preserves the original charge transfer direction while concurrently suppressing carrier recombination. Although narrow-bandgap semiconductors typically exhibit high charge recombination rates, this work demonstrates an effective strategy for significantly narrowing the band gap without compromising charge separation efficiency.

2.3 Photoreduction of CO₂ over CoPc/g-C₃N₄-P_x hybrid catalysts

Firstly, a series of control experiments were conducted to confirm that the observed products originate exclusively from the photoreduction of CO₂. These included tests under argon (Ar) atmosphere instead of CO₂, in the dark without illumination, with only CoPc (without photosensitizer), with only g-C₃N₄-P_x (without CoPc), and without any hybrid photocatalyst. Table S1 lists the results of the corresponding control experiments for CO₂ photoreduction based on CoPc/g-C₃N₄-P_{1.5} hybrid catalyst. No product was detected in argon atmosphere, in the dark, in the absence of CoPc/g-C₃N₄-P_x hybrid catalyst, or with only CoPc (without photosensitizer). Only trace CH₄ was detected with only g-C₃N₄-P_x (without CoPc) under visible-light irradiation. These results confirm that the CO originates from the photoreduction of CO₂ catalysed by the CoPc/g-C₃N₄-P_x hybrid catalyst, and CoPc itself (without a sensitizer) has no activity for CO₂ reduction under visible-light irradiation.

Under visible-light illumination (420 nm < λ < 780 nm), the prepared CoPc/g-C₃N₄-P_x hybrid catalysts show high photocatalytic activity and selectivity for CO₂ reduction CO, attributed to the intrinsic CO selectivity of CoPc. Only CO was detected, no CH₄, H₂, C₂ gas, or liquid products in CO₂ reduction based on CoPc/g-C₃N₄-P_x hybrid photocatalyst was detected. The order of performance under visible light was as follows: CoPc/g-C₃N₄-P_{1.5} (14.95 mmol g⁻¹) > CoPc/g-C₃N₄-P_{2.0} (13.85 mmol g⁻¹) > CoPc/g-C₃N₄-P_{1.0} (12.67 mmol g⁻¹) > CoPc/g-C₃N₄-P_{3.0} (8.73 mmol g⁻¹) > CoPc/g-C₃N₄-P_{0.5} (5.54 mmol g⁻¹) > CoPc/g-C₃N₄ (2.47 mmol g⁻¹) after 6 hours. The highest CO yield of 14.95 mmol g⁻¹ was achieved with the CoPc/g-C₃N₄-P_{1.5} catalyst, which is approximately 6.1 times that of the unmodified CoPc/g-C₃N₄. When pyridine was grafted onto the g-C₃N₄ framework, the CO yield initially increased significantly with increasing pyridine content. Further increasing the pyridine grafting amount resulted in a decline of photocatalytic activity. Table S2 lists the recent advances of photocatalytic reduction of CO₂ based on molecular catalyst/semiconductor hybrid photocatalyst, CoPc/g-C₃N₄-P_{1.5} hybrid catalyst exhibits competitive performance, especially in terms of CO yield based on non-noble metal molecular/g-C₃N₄ hybrid catalysts under visible-light irradiation.

To evaluate the superior stability of the CoPc/g-C₃N₄-P_{1.5} hybrid catalyst compared to the unmodified CoPc/g-C₃N₄, a continuous 12-hour CO₂ photoreduction test was conducted. As shown in Fig. S6, the time-dependent CO evolution was monitored using two catalytic systems: 50 mg of g-C₃N₄-P_{1.5} hybrid with 1.0 mg of CoPc, and 50 mg of g-C₃N₄ hybrid with 1.0 mg of CoPc, both dispersed in an acetonitrile/water/triethanolamine (CH₃CN/H₂O/TEOA) mixed solution (3:1:1, 100 mL) under visible-light irradiation. The CO yield from the CoPc/g-C₃N₄-P_{1.5} catalyst increased almost linearly over the 12-hour period, demonstrating significantly higher efficiency and durability than CoPc/g-C₃N₄. These results confirm the excellent stability of the CoPc/g-C₃N₄-P_{1.5} hybrid under visible-light conditions. It is noteworthy that the dynamic coordination bond in the CoPc/g-C₃N₄-P_{1.5} hybrid interface confers a certain self-repairing capability, thereby enhancing the overall durability of the catalytic system.

2.4 Mechanism of the enhanced photocatalytic performance

2.4.1 EIS Nyquist plots and transient photocurrent response

To elucidate the enhanced photocatalytic performance, electrochemical impedance spectroscopy (EIS) Nyquist plots and Transient photocurrent-time response (I-t) curves were recorded using g-C₃N₄ and g-C₃N₄-P_x films as working electrodes. EIS reflects the charge transfer resistance at the electrode/electrolyte interface, while the I-t curves provide further insight into the synergistic effect of light absorption and photo-generated charge separation. The impedance parameters can be derived from the spectra using equivalent circuit shown as an inset in Fig. 5a. In the equivalent circuit, R_{ct} corresponds to the charge transfer impedance. The R_{ct} values of g-C₃N₄, g-C₃N₄-P_{0.5}, g-C₃N₄-P_{1.0}, g-C₃N₄-P_{1.5}, g-C₃N₄-P_{2.0} and g-C₃N₄-P_{3.0} were fitted to be 2394, 1738, 761, 759, 768, and 1377 Ω , respectively. The R_{ct} value decreases significantly from g-C₃N₄ to g-C₃N₄-P_{1.5}, and then gradually increases from g-C₃N₄-P_{2.0} to g-C₃N₄-P_{3.0}. The smallest radius is observed for g-C₃N₄-P_{1.5}, accordingly, g-C₃N₄-P_{1.5} shows the lowest R_{ct} value and, thereby, the lowest charge transfer resistance and most efficient charge separation, which correlates well with the CO₂ photoreduction activity shown in Fig. 4d and is further supported by the transient photocurrent results below. These findings suggest that an appropriate incorporation of pyridine significantly facilitates charge separation and transfer.

Moreover, under visible light irradiation, all pyridine-modified samples (g-C₃N₄-P_x) exhibit substantially higher photocurrents than pristine g-C₃N₄ (Fig. 5b). As indicated in Fig. 4a, the enhanced visible-light absorption resulting from pyridine grafting contributes to the improved photocurrent response. The photocurrent increases progressively from g-C₃N₄ to g-C₃N₄-P_{1.5}, and then declines from g-C₃N₄-P_{1.5} to g-C₃N₄-P_{3.0}. The trend in photocurrent intensity aligns closely with the photocatalytic CO production performance (Fig. 4d), with minor discrepancies observed for g-C₃N₄-P_{1.0} and g-C₃N₄-P_{3.0}. Among all samples, g-C₃N₄-P_{1.5}



demonstrates the highest photocurrent, implying optimal synergy between light harvesting and charge separation. Therefore, appropriate edge-grafting of pyridine is an effective strategy for enhancing the photoelectrochemical properties of $g\text{-C}_3\text{N}_4$.

2.4.2 Steady-PL and TR-PL kinetics decay

Steady-state and time-resolved photoluminescence (Steady-PL and TR-PL) decay spectra were acquired with excitation at 370 nm and emission monitored at 460 nm to probe the charge carrier dynamics within the materials. As presented in Fig. 6a, both pristine $g\text{-C}_3\text{N}_4$ and pyridine-edge-functionalized $g\text{-C}_3\text{N}_4\text{-P}_x$ samples exhibit a broad fluorescence emission band. The pristine $g\text{-C}_3\text{N}_4$ demonstrates the highest emission intensity, indicative of strong radiative charge recombination. A notable quenching of the steady-PL intensity is observed across all pyridine-modified samples, particularly from $g\text{-C}_3\text{N}_4\text{-P}_{1.0}$ onward. This suppression implies significantly reduced radiative recombination, which we attribute to facilitated electron transfer via non-radiative pathways and enhanced charge separation resulting from pyridine grafting. The introduction of pyridine moieties at the framework edges likely provides charge delocalization channels and promotes interfacial electron transfer, thereby suppressing recombination.

Concurrently, a systematic red-shift in the emission peak from 453 nm ($g\text{-C}_3\text{N}_4$) to 570 nm ($g\text{-C}_3\text{N}_4\text{-P}_{3.0}$) is observed with increasing pyridine content. This red-shift reflects a narrowing of the effective bandgap due to the formation of an intramolecular donor–acceptor (D–A) structure, wherein the electron-donating pyridine units interact with the electron-accepting triazine motifs of $g\text{-C}_3\text{N}_4$. The trend aligns well with the red-shift of the absorption onset shown in Fig. 4a, corroborating the electronic modulation of the material through functionalization. These PL results collectively affirm that pyridine edge-grafting effectively alters the electronic structure of $g\text{-C}_3\text{N}_4$, facilitating charge separation and transfer—key factors underlying the enhanced photocatalytic performance.

The TR-PL decay spectra monitored at 460 nm (Fig. 6b) provide further insight into the charge transfer dynamics. All samples exhibit typical exponential decay behaviour, with the pyridine-modified $g\text{-C}_3\text{N}_4\text{-P}_x$ samples demonstrating markedly accelerated decay kinetics compared to pristine $g\text{-C}_3\text{N}_4$. Moreover, a progressive acceleration in PL decay is observed from $g\text{-C}_3\text{N}_4\text{-P}_{0.5}$ to $g\text{-C}_3\text{N}_4\text{-P}_{3.0}$. The fluorescence lifetimes were quantitatively analysed using a tri-exponential decay model, and the fitted results are summarized in Table 1. Each lifetime component (τ_1 , τ_2 , τ_3) exhibits a consistent decreasing trend with increasing pyridine content. The average fluorescence lifetime (τ_{av}) decreases sequentially from 6.11 ns (pristine $g\text{-C}_3\text{N}_4$) to 1.84 ns ($g\text{-C}_3\text{N}_4\text{-P}_{3.0}$), confirming enhanced non-radiative decay pathways.

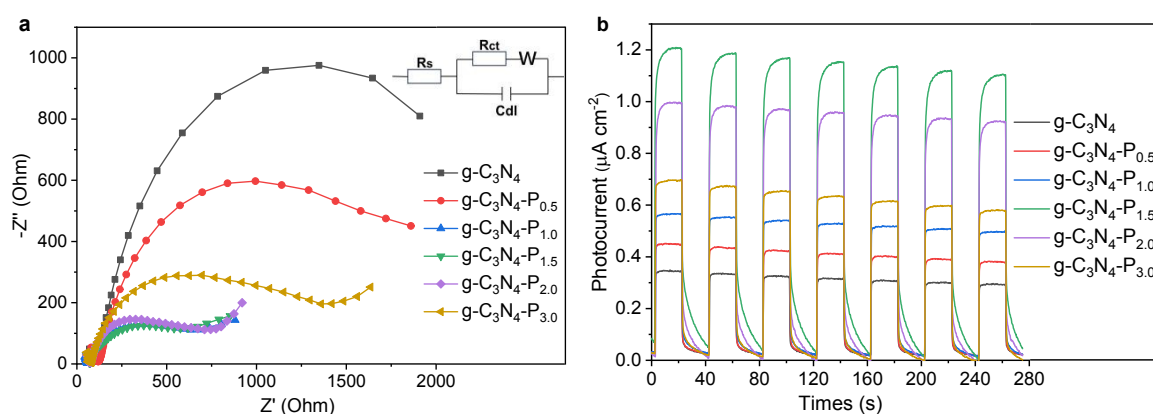


Fig. 5 (a) EIS Nyquist plots (the inset is the equivalent circuit) and (b) transient photocurrent response (I-t) of the pristine $g\text{-C}_3\text{N}_4$ and $g\text{-C}_3\text{N}_4\text{-P}_x$ ($x = 0.5 \sim 3.0$) samples.

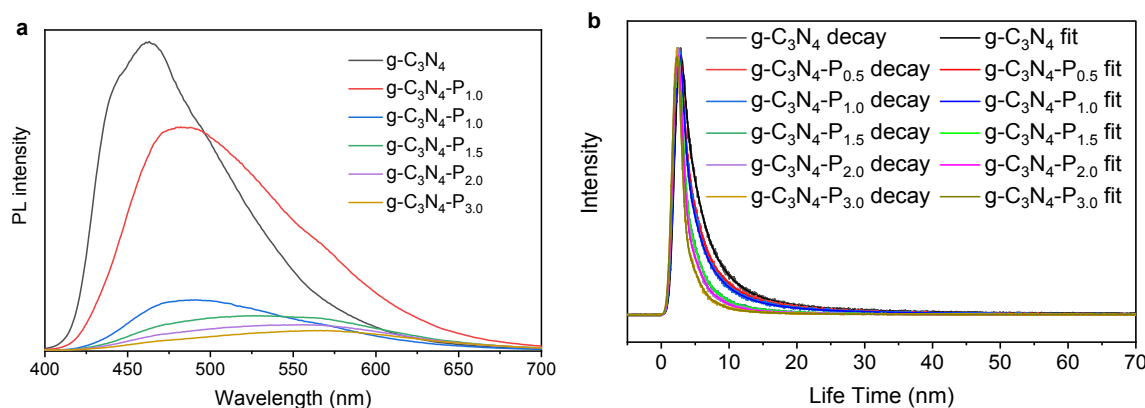


Fig. 6 (a) Steady-PL and (b) TR-PL kinetics decay spectra probed at 460 nm of the pristine $g\text{-C}_3\text{N}_4$ and as-synthesized $g\text{-C}_3\text{N}_4\text{-P}_x$ ($x = 0.5 \sim 3.0$) samples at 370 nm excitation.

Table 1. The fitted parameters of fluorescence lifetime of the as-synthesized $g\text{-C}_3\text{N}_4\text{-P}_x$ ($x = 0 \sim 3.0$) sample.



	$g\text{-C}_3\text{N}_4$	$g\text{-C}_3\text{N}_4\text{-P}_{0.5}$	$g\text{-C}_3\text{N}_4\text{-P}_{1.0}$	$g\text{-C}_3\text{N}_4\text{-P}_{1.5}$	$g\text{-C}_3\text{N}_4\text{-P}_{2.0}$	$g\text{-C}_3\text{N}_4\text{-P}_x$
τ_1 (ns)	4.03	3.70	3.40	2.66	2.58	2.07
rel. %	52.03%	44.61%	43.25%	39.82%	36.82%	31.59%
τ_2 (ns)	16.67	14.51	12.90	11.1	11.19	8.81
rel. %	22.33%	25.27%	24.72%	15.86%	12.58%	11.07%
τ_3 (ns)	1.14	0.82	0.71	0.51	0.48	0.36
rel. %	25.64%	30.12%	32.04%	44.32%	50.60%	57.34%
τ (ns)	6.11	5.56	4.89	3.05	2.60	1.84

This systematic reduction in lifetime reflects more efficient electron transfer from the $g\text{-C}_3\text{N}_4$ matrix to the pyridine functional groups at the material's edge. The introduced pyridine rings likely serve as electron-accepting sites, facilitating rapid separation and extraction of photo-generated electrons, thereby suppressing radiative recombination. Together, the steady-state and time-resolved PL results conclusively demonstrate that pyridine edge-functionalization promotes the separation of photo-induced electron-hole pairs and inhibits their recombination.

2.4.3 Theoretical calculation

To gain deeper mechanistic insights into how pyridine edge-grafting enhances the photocatalytic performance and charge separation in $g\text{-C}_3\text{N}_4\text{-P}_x$, density functional theory (DFT) calculations were performed to evaluate the molecular dipole moment and the electron density distribution of the highest occupied molecular orbitals (HOMO) and the lowest unoccupied molecular orbitals (LUMO). The molecular model of $g\text{-C}_3\text{N}_4$ was constructed using three connected 3-s-triazine units, while the $g\text{-C}_3\text{N}_4\text{-P}_x$ model was built by grafting one pyridine ring onto the terminal triazine unit. As shown in Fig. 7, the optimized structures, computed dipole moments, and spatial distributions of the HOMO and LUMO orbitals are compared between $g\text{-C}_3\text{N}_4$ and $g\text{-C}_3\text{N}_4\text{-P}_x$. The dipole moment increases from 4.75 Debye in $g\text{-C}_3\text{N}_4$ to 5.47 Debye in $g\text{-C}_3\text{N}_4\text{-P}_x$, indicating enhanced molecular polarity induced by pyridine functionalization. This greater polarity facilitates improved charge separation and promotes more efficient charge transport within the material.

Orbital analysis in Fig. 7 reveals that in pristine $g\text{-C}_3\text{N}_4$, the HOMO is delocalized evenly across all three triazine units, whereas the LUMO is predominantly localized on two of the triazine units. In contrast, for $g\text{-C}_3\text{N}_4\text{-P}_x$, the HOMO is mainly distributed over the two triazine units distal to the pyridine group, with minimal contribution from the pyridine-linked triazine and none from the pyridine itself. The LUMO, however, is primarily located on the pyridine-anchored triazine unit, with additional density extending into the pyridine ring and the remaining triazine motifs. The frontier molecular orbitals, HOMO and LUMO, correspond to bonding and anti-bonding orbitals, respectively, and dictate the spatial distribution of holes and electrons upon photoexcitation. Compared with pristine $g\text{-C}_3\text{N}_4$, the isodensity surface plots of $g\text{-C}_3\text{N}_4\text{-P}_x$ reveal a more pronounced and directional shift of

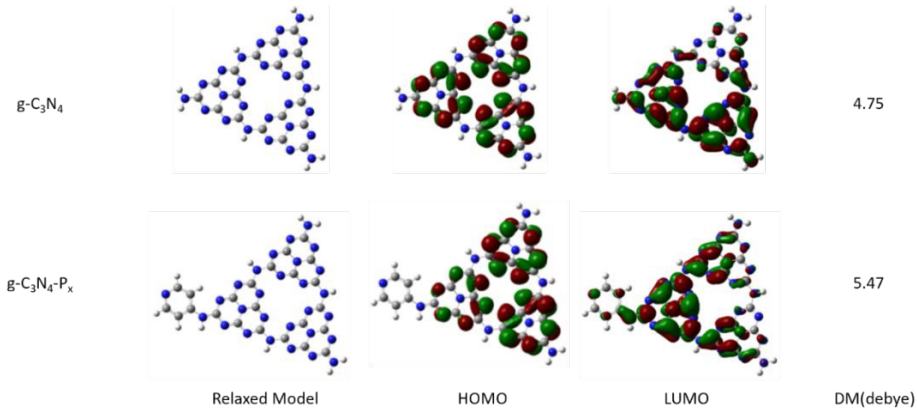
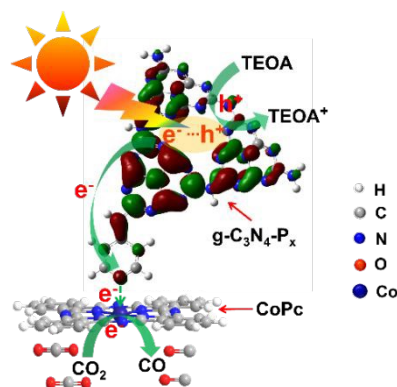


Fig. 7 Optimized structure, calculated dipole moment, isodensity surface plots of the HOMO and LUMO for $g\text{-C}_3\text{N}_4$ and $g\text{-C}_3\text{N}_4\text{-P}_x$ model structure.



View Article Online
DOI: 10.1039/D5IM00296F

Scheme 1 Charge transfer diagram for CO₂ photoreduction over CoPc/g-C₃N₄-P_x hybrid photocatalysts under visible-light illumination.

electron density from the 3-s-triazine core toward the edge-anchored pyridine ring under excitation. This redistribution supports efficient photoinduced electron transfer from the central region to the peripheral functional groups, thereby facilitating charge separation and reducing the likelihood of electron–hole recombination. The DFT simulation results align consistently with the fluorescence spectra discussed above.

2.4.4 Mechanism of the optimum photocatalytic performance at P_{1.5}

Thermodynamically, all g-C₃N₄-P_x samples can transfer electrons to CoPc [$E_{CB} = -1.19$ to -1.26 V vs. NHE; $E_{red(CoPc)} \approx -0.90$ V vs. NHE,⁵⁰ satisfying the requirement for CO₂ reduction ($E_{(CO_2/CO)} = -0.52$ V vs. NHE). The slight variation in E_{CB} (0.02 – 0.07 eV) among g-C₃N₄-P_x samples implies negligible differences in driving force for electron transfer, indicating that the enhanced activity does not originate from thermodynamic factors. The charge transfer diagram for CO₂ photoreduction over CoPc/g-C₃N₄-P_x hybrid catalysts is proposed in Scheme 1. Firstly, photoexcitation of g-C₃N₄-P_x generates electron–hole pairs; Secondly, electrons transfer efficiently to CoPc via pyridine bridges and holes migrate to the g-C₃N₄-P_x surface, competing with recombination; Finally, CO₂ is reduced to CO at CoPc sites, meanwhile, the holes are scavenged by the sacrificial agent TEOA. As shown in Fig. 4d, the photocatalytic activity of CoPc/g-C₃N₄-P_x depends strongly on the pyridine grafting level (x). The CO₂ reduction performance increases with pyridine loading up to an optimum at x = 1.5, beyond which it declines. This trend can be explained by the interplay of several key factors:

The performance optimum at P_{1.5} reflects a kinetic spot between enhanced charge separation and competing recombination pathways. At lower loadings (x < 1.5), increasing pyridine content improves visible-light absorption, facilitates in-plane charge separation within g-C₃N₄, and promotes directional electron transfer from g-C₃N₄-P_x to CoPc. This is supported by the lowest charge-transfer resistance (Fig. 5a) and highest photocurrent response (Fig. 5b) observed at P_{1.5}. However, further increasing the pyridine loading beyond this point introduces excessive surface defects or states that act as charge recombination centres, as indicated by the increased charge-transfer resistance and decreased photocurrent. These defects promote electron–hole recombination before electrons can reach the CoPc active sites. In addition, excessive pyridine functionalization leads to an overly elevated valence band maximum (E_{VB} in Fig. 4c), which reduces the hole oxidation power and weakens the anode half-reaction, thereby impairing catalyst regeneration. Moreover, while an optimal pyridine content enables efficient coordination and electron transfer to CoPc, an excess may cause non-productive coordination or steric hindrance, blocking active sites and leading to local electron accumulation. This imbalance between pyridine and CoPc promotes recombination instead of catalysis, ultimately lowering the CO₂ reduction efficiency.^{51,52}

3. Conclusions

In conclusion, we have successfully synthesized pyridine edge-functionalized g-C₃N₄-P_x coupled with CoPc for efficient photocatalytic CO₂ reduction to CO under visible light. In this hybrid system, g-C₃N₄-P_x serves as a light-harvesting unit while CoPc acts as the catalytic sites for CO₂ reduction. The grafting of electron withdrawing pyridine groups enhances visible-light absorption, promotes directional in-plane charge separation within g-C₃N₄. Unlike conventional CoPc/g-C₃N₄ systems, which primarily rely on physical adsorption, static interactions, or direct covalent linking, our work introduces polarization engineering and coordination via pyridine edge-functionalization. This approach not only promote the in-plane charge separation within g-C₃N₄, for improved light absorption but also enables directional electron transfer and reversible coordination between g-C₃N₄ and CoPc, significantly boosting charge separation and CO₂ reduction performance. The optimal catalyst, CoPc/g-C₃N₄-P_{1.5}, achieves a CO yield of 14.95 mmol g⁻¹ after 6 h of visible light irradiation, which is 6.1 times higher than that of the non-functionalized counterpart. The improvement of photocatalytic activity is mainly due to the increase of electron velocity between photosensitizer and catalyst, which emphasizes the superiority of directional electron transfer and constructing dynamic coordination interaction. The one-step thermal polymerization used for g-C₃N₄-P_x is simple, scalable, and based on low-cost precursors, the coordination with CoPc is also straightforward and conducted under mild conditions, making the CoPc/g-C₃N₄-P_x hybrid suitable for large-scale production. This



work offers a strategic guideline for designing efficient semiconductor–molecular hybrid photocatalysts for CO₂ conversion into solar fuel.

DOI: 10.1039/D5IM00296F

4. Experimental section

4.1 Regents

All the reagents and solvents were chromatographic or analytical grade. Urea, 4-aminopyridine, TEOA, CH₃CN, and N,N-dimethylformamide (DMF) were purchased from Shanghai Aladdin Bio-chem Technology. Tetraethylammonium tetrafluoroborate (Et₄NBF₄) were obtained from Sigma-Aldrich. CO₂ with purity of 99.999% was bought from Shanxi Beiwen Gases Company. Ultrapure water (Millipore Milli-Q grade, 18.2 MΩ cm) was used in all the experiments.

4.2 Synthesis

Pristine g-C₃N₄ was synthesized by directly thermal polymerization of urea at 560 °C for 4 h with a heating rate of 2.5 °C min⁻¹ in a lidded alumina crucible in muffle furnace with ambient atmosphere. The pyridine edge-functionalized g-C₃N₄-P_x samples were prepared through thermal polymerization of urea with different amount of 4-aminopyridine as the synthetic process of g-C₃N₄. The edge-grafted amount of pyridine in final g-C₃N₄-P_x composites was altered via changing the quantity of 4-aminopyridine used in thermal polymerization. The g-C₃N₄-P_x samples synthesized with 4-aminopyridine to urea weight percentage of 0.5 %, 1.0 %, 1.5 %, 2.0 %, and 3.0 % was denoted as g-C₃N₄-P_{0.5}, g-C₃N₄-P_{1.0}, g-C₃N₄-P_{1.5}, g-C₃N₄-P_{2.0}, and g-C₃N₄-P_{3.0}, respectively.

CoPc was synthesized and characterized as previously reported.⁵³ The CoPc/g-C₃N₄-P_x hybrid catalysts were prepared by integrating 1 mg of CoPc with 50 mg g-C₃N₄-P_x under stirring overnight in 100 mL solution of acetonitrile/water/TEOA (3:1:1, v:v:v). FT-IR spectra were measured to verify the CoPc/g-C₃N₄-P_{1.5} heterogeneous catalyst (Fig. S6).

4.3 Characterization

Morphology of the g-C₃N₄-P_x samples was observed on Hitachi S4800 field emission SEM and FEI Tecnai G2 T20 TEM. XRD was measured on Bruker D8 diffractometer with Cu Kα radiation. The BET specific surface area was measured by a surface area and porosity analyser (Micromeritics, Tristar II 3020). XPS was carried out on ESCALAB 250Xi X-ray photoelectron spectrometer. UV–vis DRS was recorded on Lambda 750 UV/Vis/NIR spectrophotometer (Perkin-Elmer, USA) using BaSO₄ as background. Steady-PL and TR-PL decay spectra excited at 370 nm were collected on a NanoLOG-TCSPC spectrophotometer (Horiba Jobin Yvon, USA). Transient I-t curves and Mott-Schottky plots were tested with a frequency of 1 kHz. EIS measurements were performed under an ac amplitude of 10 mV with a frequency range from 10⁻¹ Hz to 10⁵ Hz. All of the photoelectrochemical measurements were performed in a three-electrode cell on CHI 660D potentiostat (Shanghai Chenhua) in DMF solution using 0.1 M of Et₄NBF₄ as the electrolyte. g-C₃N₄-P_x films on FTO glass, Pt sheet and Ag/AgCl were used as working, counter and reference electrode, respectively.

4.4 Photocatalytic CO₂ reduction

Photoreduction of CO₂ was performed over CoPc/g-C₃N₄-P_x hybrid photocatalysts in CH₃CN:H₂O:TEOA (3:1:1, 100 mL) mixed solution in a photoreaction system (Labsolar-IIIAG, Beijing Perfect Light Technology Co., Ltd.) saturated with 28 kPa CO₂ at 15 °C as reported.¹¹ The volume of the reactor was 250 mL, and the volume of the gas circulation pipeline was 150 mL. The CoPc/g-C₃N₄-P_x hybrid catalysts were prepared by integrating 1 mg CoPc with 50 mg g-C₃N₄-P_x under stirring overnight in 100 mL solution of acetonitrile/water/TEOA (3:1:1, v:v:v) in advance. The photoreaction system was vacuumed and purged with high purity CO₂ gas for 1 h before illumination. The reactor was illuminated under visible light (420 nm < λ < 780 nm) using a 300 W Xe lamp (Microsolar 300, Beijing Perfect Light Technology Co., Ltd.) with a 420 nm cut off filter and an 780 nm IR-cut filter. The spot diameter is 60 mm and the irradiation height is 10 cm. The light intensity was calibrated using a silicon photodiode power meter, which was 280 mW cm⁻². The total photon flux was calculated to be approximately 1.26*10⁻⁶ photons s⁻¹ m⁻². The spectrum of Microsolar 300 Xe light (420 nm < λ < 780 nm) was shown in Fig. S7. The gas reduction products were analysed by using Agilent 7890A gas chromatography equipped with a hydrogen flame ionized detector (FID) and a thermal conductivity detector (TCD) using He as the carrier gas. The FID detector was fitted with a methanizer to detect CO. The typical chromatographic curve of CH₄ and CO with residence time and GC calibration curve were shown on Fig. S8 and Fig. S9, respectively. A series of control experiments (i.e. purging Ar instead of CO₂, under dark without illumination, only CoPc without photosensitizer, only g-C₃N₄-P_x without CoPc, and without the hybrid photocatalyst) were carried out.

4.5 Theoretical calculation

Theoretical calculation was carried out on Gaussian using DFT method.⁵⁴ Becke's three-parameter hybrid functional with the LYP correlation functional (B3LYP) together with 6-31G(d) basis set was employed. Geometry optimization and electronic properties of g-C₃N₄ and g-C₃N₄-P_x models with the minimum energy conformation were carried out without any symmetry constraint. The molecular dipole moment and electron distribution of the HOMO and LUMO were obtained.

Author Contributions

Xuehua Zhang: Resources, Methodology, Formal analysis, Data curation, Writing – original draft. Chunlei Su: Resources, Formal analysis, Data curation. Rui Shi: Data curation. Mingming Li: Methodology. Lili Fu: Formal analysis. Rongji Liu: Methodology, Investigation. Yong Chen: Writing – review & editing, Visualization, Validation. Bin Li: Formal analysis, review & editing, Funding acquisition. Guangjin Zhang: Formal analysis, Writing – review & editing, Supervision, Funding acquisition and Project administration.



ARTICLE

Industrial Chemistry & Materials

Conflicts of interest

The authors declare no conflict of interest.

View Article Online
DOI: 10.1039/D5IM00296F

Data availability

The data supporting this article have been included as part of the Supplementary Information.†

Acknowledgements

This work is supported by the National Natural Science Foundation of China (22378402; 22178361), the International Partnership Project of CAS (039GJHZ2022029GC), Fundamental research project of China National Tobacco Corporation (No. 110202403002) and the Major Project of the Innovation Platform at the Key Laboratory of Tobacco Processing Technology, State Tobacco Monopoly Administration (CNTC, 202025AWCX01).

References

1. T. Inoue, A. Fujishima, S. Konishi and K. Honda, Photoelectrocatalytic reduction of carbon dioxide in aqueous suspensions of semiconductor powders, *Nature*, 1979, **277**, 637–638.
2. W. Tu, Y. Zhou and Z. Zou, Photocatalytic conversion of CO₂ into renewable hydrocarbon fuels: State-of-the-art accomplishment, challenges, and prospects, *Adv. Mater.*, 2014, **26**, 4607–4626.
3. X. Li, J. Yu, M. Jaroniec and X. Chen, Cocatalysts for selective photoreduction of CO₂ into solar fuels, *Chem. Rev.*, 2019, **119**, 3962–4179.
4. Y. Wang, E. Chen and J. Tang, Insight on reaction pathways of photocatalytic CO₂ conversion, *ACS Catal.*, 2022, **12**, 7300–7316.
5. C. Huang, X. Zhang, D. Li, M. Wang and Q. Wu, The influence of the precursor molar ratio on the structure of the CdS catalyst during synthesis and visible-light driven CO₂ reduction into solar fuel, *New J. Chem.*, 2022, **46**, 10339–10346.
6. D. Zhang and H. Wang, Polyoxometalate-based nanostructures for electrocatalytic and photocatalytic CO₂ reduction, *Polyoxometalates*, 2022, **1**, 9140006.
7. T. Morikawa, S. Sato, K. Sekizawa, T. Suzuki and T. Arai, Solar-driven CO₂ reduction using a semiconductor/molecule hybrid photosystem: From photocatalysts to a monolithic artificial leaf, *Acc. Chem. Res.*, 2022, **55**, 933–943.
8. S. Zhang, R. Liu, C. Streb and G. Zhang, Design and synthesis of novel polyoxometalate-based binary and ternary nanohybrids for energy conversion and storage, *Polyoxometalates*, 2023, **2**, 9140037.
9. R. Kuriki, K. Sekizawa, O. Ishitani and K. Maeda, Visible-light-driven CO₂ reduction with carbon nitride: Enhancing the activity of ruthenium catalysts, *Angew. Chem. Int. Ed.*, 2015, **54**, 2406–2409.
10. G. Zhao, H. Pang, G. Liu, P. Li, H. Liu, H. Zhang, L. Shi and J. Ye, Co-porphyrin/carbon nitride hybrids for improved photocatalytic CO₂ reduction under visible light, *Appl. Catal. B: Environ.*, 2017, **200**, 141–149.
11. L. Lin, C. Hou, X. Zhang, Y. Wang, Y. Chen and T. He, Highly efficient visible-light driven photocatalytic reduction of CO₂ over g-C₃N₄ nanosheets/tetra(4-carboxyphenyl)porphyrin iron(III) chloride heterogeneous catalysts, *Appl. Catal. B: Environ.*, 2018, **221**, 312–319.
12. X. Zhang, L. Lin, D. Qu, J. Yang, Y. Wang, Z. Wang, Z. Sun, Y. Chen and T. He, Boosting visible-light driven solar-fuel production over g-C₃N₄/tetra(4-carboxyphenyl)porphyrin iron(III) chloride hybrid photocatalyst via incorporation with carbon dots, *Appl. Catal. B: Environ.*, 2020, **265**, 118595.
13. B. Ma, G. Chen, C. Fave, L. Chen, R. Kuriki, K. Maeda, O. Ishitani, T.-C. Lau, J. Bonin and M. Robert, Efficient visible-light-driven CO₂ reduction by a cobalt molecular catalyst covalently linked to mesoporous carbon nitride, *J. Am. Chem. Soc.*, 2020, **142**, 6188–6195.
14. Y. Wei, L. Chen, H. Chen, L. Cai, G. Tan, Y. Qiu, Q. Xiang, G. Chen, T.-C. Lau and M. Robert, Highly efficient photocatalytic reduction of CO₂ to CO by in situ formation of a hybrid catalytic system based on molecular iron quaterpyridine covalently linked to carbon nitride, *Angew. Chem. Int. Ed.*, 2022, **61**, e202116832.
15. P. Li, C. Hou, X. Zhang, Y. Chen and T. He, Ethylenediamine-functionalized CdS/tetra(4-carboxyphenyl)porphyrin iron (III) chloride hybrid system for enhanced CO₂ photoreduction, *Appl. Surf. Sci.*, 2018, **459**, 292–299.
16. P. Li, X. Zhang, C. Hou, L. Lin, Y. Chen and T. He, Visible-light-driven CO₂ photoreduction over Zn_xCd_{1-x}S solid solution coupling with tetra(4-carboxyphenyl)porphyrin iron(III) chloride, *Phys. Chem. Chem. Phys.*, 2018, **20**, 16985–16991.
17. P. Li, X. Zhang, C. Hou, Y. Chen and T. He, Highly efficient visible-light driven solar-fuel production over tetra(4-carboxyphenyl)porphyrin iron(III) chloride using CdS/Bi₂S₃ heterostructure as photosensitizer, *Appl. Catal. B: Environ.*, 2018, **238**, 656–663.
18. A. Perazio, G. Lowe, R. Gobetto, J. Bonin and M. Robert, Light-driven catalytic conversion of CO₂ with heterogenized molecular catalysts based on fourth period transition metals, *Coord. Chem. Rev.*, 2021, **443**, 214018.
19. F. Arcudi, L. Đorđević, B. Nagasing, S. I. Stupp and E.A. Weiss, Quantum dot-sensitized photoreduction of CO₂ in water with turnover number >80,000, *J. Am. Chem. Soc.*, 2021, **143**, 18131–18138.
20. J. Wang, L. Jiang, H. Huang, Z. Han and G. Ouyang, Rapid electron transfer via dynamic coordinative interaction boosts quantum efficiency for photocatalytic CO₂ reduction, *Nat. Commun.*, 2021, **12**, 4276.
21. J. Bian, J. Feng, Z. Zhang, Z. Li, Y. Zhang, Y. Liu, S. Ali, Y. Qu, L. Bai, J. Xie, D. Tang, X. Li, F. Bai, J. Tang and L. Jing, Dimension-matched zinc phthalocyanine/BiVO₄ ultrathin nanocomposites for CO₂ reduction as efficient wide-visible-light-driven photocatalysts via a cascade charge transfer, *Angew. Chem. Int. Ed.*, 2019, **58**, 10873–10878.
22. J. Sun, J. Bian, J. Li, Z. Zhang, Z. Li, Y. Qu, L. Bai, Z. Yang and L. Jing, Efficient photocatalytic conversion of CO₂ on ultrathin metal phthalocyanine/g-C₃N₄ heterojunctions by promoting charge transfer and CO₂ activation, *Appl. Catal. B: Environ.*, 2020, **277**, 119199.
23. S. Xu, X. Li, S. Li, H. Rao, J.-S. Qin, P. She, W.-C. Cheong and L. Jing, Recent advances of photocatalytic CO₂ reduction based on hybrid molecular catalyst/semiconductor photocatalysts: A review, *Small*, 2025, **21**, 2408075.



24. S. McGuigan, S. J. Tereniak, C. L. Donley, A. Smith, S. Jeon, F. Zhao, R. N. Sampaio, M. Pauly, L. Keller, L. Collins, G. N. Parsons, T. Lian, E. A. Stach and P. A. Maggard, Discovery of a hybrid system for photocatalytic CO₂ reduction via attachment of a molecular cobalt-quaterpyridine complex to a crystalline carbon nitride, *ACS Appl. Energy Mater.*, 2023, **6**, 10542–10555. DOI: 10.1039/D3SM00258F
25. Y.-H. Li, Y. Chen, J.-Y. Guo, R. Wang, S.-N. Zhao, G. Li and S.-Q. Zang, Engineering coordination microenvironments of polypyridine Ni catalysts embedded in covalent organic frameworks for efficient CO₂ photoreduction, *Chin. J. Catal.*, 2025, **74**, 155–166.
26. J.-W. Wang, F. Zhao, H.-H. Huang, Z. Han and G. Ouyang, Molecular catalyst coordinatively bonded to organic semiconductors for selective light-driven CO₂ reduction in water, *Nat. Commun.*, 2024, **15**, 9779.
27. M. Schulz, M. Karnahl, M. Schwalbe and J. Vos, The role of the bridging ligand in photocatalytic supramolecular assemblies for the reduction of protons and carbon dioxide, *Coord. Chem. Rev.*, 2012, **256**, 1682–1705.
28. X. Wang, K. Maeda, A. Thomas, K. Takanabe, G. Xin, J.M. Carlsson, K. Domen and M. Antonietti, A metal-free polymeric photocatalyst for hydrogen production from water under visible light, *Nat. Mater.*, 2009, **8**, 76–80.
29. W. Ong, L. Tan, Y. Ng, S. Yong and S. Chai, Graphitic carbon nitride (g-C₃N₄)-based photocatalysts for artificial photosynthesis and environmental remediation: Are we a step closer to achieving sustainability? *Chem. Rev.*, 2016, **116**, 7159–7329.
30. J. Wen, J. Xie, X. Chen and X. Li, A review on g-C₃N₄-based photocatalysts, *Appl. Surf. Sci.*, 2017, **391**, 72–123.
31. R. Umapathi, C. V. Raju, S. M. Ghoreishian, G. M. Rani, K. Kumar, M.-H. Oh, J. P. Park and Y. S. Huh, Recent advances in the use of graphitic carbon nitride-based composites for the electrochemical detection of hazardous contaminants, *Coord. Chem. Rev.*, 2022, **470**, 214708.
32. S. M. Ghoreishian, K. S. Ranjith, M. Ghasemi, B. Park, S.-K. Hwang, N. Irannejad, M. Norouzi, S. Y. Park, R. Behjatmanesh-Ardakani, S. M. Pourmortazavi, S. Mirsadeghi, Y.-K. Han and Y. S. Huh, Engineering the photocatalytic performance of B-C₃N₄@Bi₂S₃ hybrid heterostructures for full-spectrum-driven Cr(VI) reduction and in-situ H₂O₂ generation: Experimental and DFT studies, *Chem. Eng. J.*, 2023, **452**, 139435.
33. Y. Li, T. Kong and S. Shen, Artificial photosynthesis with polymeric carbon nitride: When meeting metal nanoparticles, single atoms, and molecular complexes, *Small*, 2019, **15**, 1900772.
34. Q. Chen, S. Li, H. Xu, G. Wang, Y. Qu, P. Zhu and D. Wang, Co-MOF as an electron donor for promoting visible-light photoactivities of g-C₃N₄ nanosheets for CO₂ reduction, *Chin. J. Catal.*, 2020, **41**, 514–523.
35. Q. Chen, G. Gao, Y. Zhang, Y. Li, H. Zhu, P. Zhu, Y. Qu, G. Wang and W. Qin, Dual functions of CO₂ molecular activation and 4f levels as electron transport bridges in erbium single atom composite photocatalysts therefore enhancing visible-light photoactivities, *J. Mater. Chem. A*, 2021, **9**, 15820–15826.
36. C. Li, H. Wu, D. Zhu, T. Zhou, M. Yan, G. Chen, J. Sun, G. Dai, F. Ge and H. Dong, High-efficient charge separation driven directionally by pyridine rings grafted on carbon nitride edge for boosting photocatalytic hydrogen evolution, *Appl. Catal. B: Environ.*, 2021, **297**, 120433.
37. Z. Ma, X. Zong, Q. Hong, L. Niu, T. Yang, W. Jiang, D. Qu, L. An, X. Wang, Z. Kang and Z. Sun, Electrostatic potential of the incorporated asymmetry molecules induced high charge separation efficiency of the modified carbon nitride copolymers, *Appl. Catal. B: Environ.*, 2022, **319**, 121922.
38. Q. Zhang, J. Chen, H. Che, P. Wang, B. Liu and Y. Ao, Recent advances in g-C₃N₄-based donor–acceptor photocatalysts for photocatalytic hydrogen evolution: An exquisite molecular structure engineering, *ACS Mater. Lett.*, 2022, **4**, 2166–2186.
39. Y. Wu, Z. Jiang, X. Lu, Y. Liang and H. Wang, Domino electroreduction of CO₂ to methanol on a molecular catalyst, *Nature*, 2019, **575**, 639–642.
40. S. Ren, D. Joulié, D. Salvatore, K. Torbensen, M. Wang, M. Robert and C. Berlinguette, Molecular electrocatalysts can mediate fast, selective CO₂ reduction in a flow cell, *Science*, 2019, **365**, 367–369.
41. W. W. Kramer and C. C. L. McCrory, Polymer coordination promotes selective CO₂ reduction by cobalt phthalocyanine, *Chem. Sci.*, 2016, **7**, 2506–2515.
42. K. E. R. Cruz, Y. Liu, T. L. Soucy, P. M. Zimmerman and C. C. L. McCrory, Increasing the CO₂ reduction activity of cobalt phthalocyanine by modulating the σ-donor strength of axially coordinating ligands, *ACS Catal.*, 2021, **11**, 13203–13216.
43. T. L. Soucy, W. S. Dean, J. Zhou, K. E. R. Cruz and C. C. L. McCrory, Considering the influence of polymer–catalyst interactions on the chemical microenvironment of electrocatalysts for the CO₂ reduction reaction, *Acc. Chem. Res.*, 2022, **55**, 252–261.
44. H. Niu, Y. Liu, B. Mao, N. Xin, H. Jia and W. Shi, In-situ embedding MOFs-derived copper sulfide polyhedrons in carbon nanotube networks for hybrid supercapacitor with superior energy density, *Electrochim. Acta*, 2020, **329**, 135130.
45. Z. Lin and X. Wang, Nanostructure engineering and doping of conjugated carbon nitride semiconductors for hydrogen photosynthesis, *Angew. Chem. Int. Ed.*, 2013, **52**, 1735–1738.
46. S. Morrison, *Electrochemistry at semiconductor and oxidized metal electrodes*, Plenum Press, New York, 1980.
47. A. Ishikawa, T. Takata, J. Kondo, M. Hara, H. Kobayashi and K. Domen, Oxysulfide Sm₂Ti₂S₂O₅ as a stable photocatalyst for water oxidation and reduction under visible light irradiation (λ ≤ 650 nm), *J. Am. Chem. Soc.*, 2002, **124**, 13547–13553.
48. Y. Matsumoto, Energy positions of oxide semiconductors and photocatalysis with iron complex oxides, *J. Solid State Chem.*, 1996, **126**, 227–234.
49. Y. Matsumoto, K. Omae, I. Watanabe and E. Sato, Photoelectrochemical properties of the Zn-Ti-Fe spinel oxides, *J. Electrochem. Soc.*, 1986, **133**, 711–715.
50. S. Roy and E. Reisner, Visible-light-driven CO₂ reduction by mesoporous carbon nitride modified with polymeric cobalt phthalocyanine, *Angew. Chem. Int. Ed.*, 2019, **58**, 12180–12184.
51. S. M. Ghoreishian, K. S. Ranjith, H. Lee, H. Ju, S. Z. Nikoo, Y.-K. Han and Y. S. Huh, Hierarchical N-doped TiO₂@Bi₂W_xMo_{1-x}O₆ core-shell nanofibers for boosting visible-light-driven photocatalytic and photoelectrochemical activities, *J. Hazard. Mater.*, 2020, **391**, 122249.
52. S. M. Ghoreishian, K. S. Ranjith, B. Park, S.-K. Hwang, R. Hosseini, R. Behjatmanesh-Ardakani, S. M. Pourmortazavi, H. U. Lee, B. Son, S. Mirsadeghi, Y.-K. Han and Y. S. Huh, Full-spectrum-responsive Bi₂S₃@CdS S-scheme heterostructure with intimated ultrathin RGO toward photocatalytic Cr(VI) reduction and H₂O₂ production: Experimental and DFT studies, *Chem. Eng. J.*, 2021, **419**, 129530.
53. F. Moser and A. Thomas, *The Phthalocyanines*, Vol. II: Properties, CRC Press, Boca Raton, 1983.
54. M. Frisch, et al., Gaussian 09, Revision D.01, Gaussian, Inc., Wallingford CT, 2016.



View Article Online
DOI: 10.1039/D5IM00296F

Data availability

The data supporting this article have been included as part of the Supplementary Information.†

